Draft version May 3, 2025
Typeset using LaTeX **default** style in AASTeX7

Optimizing HST High-Contrast Imaging Observations of a Planet-Forming Disk

Sawyer Tabor[1] and Yifan Zhou[1]

[1] *University of Virginia*

ABSTRACT

Recent developments in direct imaging of young stellar objects have unveiled actively forming planets and various complex structures in protoplanetary disks, which could be advance indicators of ongoing planet formation. However, due to factors such as imperfect PSF subtraction and retention of disk flux, it has proven difficult to quantize the confidence of direct imaging detections. We present Hubble Space Telescope direct imaging data of RX J1604.3-2130 and demonstrate a set of image processing techniques that allow us to robustly identify the disk's features. We have performed both Angular and Reference Differential Imaging (ADI, RDI) on these data in order to remove the stellar flux and probe the faint disk and potential protoplanet candidates. After thorough exploration of relevant parameters that can affect subtraction results, we developed a robust criterion to optimize the signal-to-noise ratio of potential planetary signals, and now present a tool that can replicate these results for general use. Through the injection and recovery of physically-motivated models of accreting protoplanets, we show that it is likely that a Jupiter-mass protoplanet accreting at 10^{-8} Jupiter masses per year is detectable. These images also reveal interesting geometric structures that could trace the formation of planets.

Keywords: Direct Imaging (387) — Protoplanetary Disks (1300) — Exoplanet Formation (492) — Hubble Space Telescope (761) — Astronomy Software (1855)

1. INTRODUCTION

Despite considerable developments in the detection and characterization of exoplanets, there are large gaps in our knowledge of the mechanisms underlying planet formation, and developing a solid understanding of how matter is transported within protoplanetary disks — constraining accretion rates and planetary evolution timescales — remains an open problem. While directly imaging the process of planet formation gives the most robust test of theoretical models, the technique has only unambiguously resolved a few targets, namely, the PDS 70 system and the more controversial AB Aurigae (M. Keppler et al. (2018), S. Y. Haffert et al. (2019), A. Boccaletti et al. (2020)). Disks that feature prominent non-detections, however, still contain features that are best explained by the existence of as-yet unseen planets, such as central large gaps swept out by planetary accretion and the creation of strictly cordoned dust traps in the so-called "transition disks" (M. de Juan Ovelar et al. (2013), L. M. Close (2020)).

In particular, the transition disk surrounding the dipper star RX J1604.3-2130 (henceforth, 'J1604') has become an object of increasing interest in recent years, as the outer disk has a favorable face-on inclination and recent near-infrared ground-based observations, such as those achieved by SPHERE (P. Pinilla et al. 2018), have revealed the highly evolved disk to have additional complications in its morphology. A $4M_{\rm jup}$ protoplanet was deemed necessary to produce the large dust gap present in polarimetric differential images of the system, while kinematic analyses of the disk (J. Stadler et al. 2023) support the conclusion that a protoplanetary companion located at 41 ± 10 AU could be responsible for the observed features. However, no confirmed planetary candidate has been identified at this time, and new methods must be developed to probe the inner dust gap for evidence of this object.

Observations of planet-forming disks are often complicated by the high contrast ratio present between stellar point spread functions (PSFs) and any disk structures or planets within their associated disks. Recently, principal component analysis (PCA) has been applied to this issue, allowing for the retrieval of high-contrast images obtained by modeling and then subtracting out stellar PSFs. However, implementations of this process, such as `PynPoint` (T. Stolker et al.

Email: pcn8bk@virginia.edu, yzhou@virginia.edu

2019) and `pyKLIP` (J. J. Wang et al. 2015), remain highly sensitive to conditions such as disk geometry and subtraction parameters, and some signal may be astrophysical, but may not be a planet. Thus, our ability to produce images of astrophysical sources in disks with a sufficient signal-to-noise ratio has proven haphazard.

These subtraction parameters: movement (`movement`), annulus count / annulus spacing (`nAnnuli`), and basis vector count (`numbasis`), each contribute significant features to the subtracted PSF. Over-fit the system, and too much of the disk signal will be treated as part of the stellar PSF and be subsequently subtracted out, leading to non-detections where the only significant features in the image are noise. Under-fit the system, and not enough of the stellar PSF will be subtracted, leading to saturated results where non-physical remnants of the stellar PSF dominate. To obtain the highest quality results, there must exist some optimal combination of these parameters, which can be found by iterating over each parameter and calculating an expectation value for signal-to-noise. These techniques were first presented for ground-based data by J. I. Adams Redai et al. (2023). For application to the general case space-based data, we developed a simple Python library, KLIPtonite, which was used to determine the optimal set of subtraction parameters for an analysis of the morphology of J1604 in the Hα wavelength.

2. OBSERVATIONS

Data was sourced from the Hubble Space Telescope observing program GO-16651, which targeted 10 wide-gap transition disks in the narrow-band Hα filter F656N ($\lambda_c = 6561$ Å, FWHM= 18 Å). The Hα wavelength was chosen to best observe the hot accretion shocks generated by protoplanets, which are directly correlated with those protoplanets' accretion rates, allowing for physical models of the systems (Y. Zhou et al. 2014). Targets were selected based on their ALMA dust continuum images (L. Francis & N. van der Marel 2020) for their disk and gap sizes, disk orientations, stellar brightnesses, and stellar mass accretion rates, in order to achieve the lowest contrast ratio of accreting protoplanets in the selected systems and the highest probability of detecting unseen protoplanets.

Each target was observed with two telescope roll angles to facilitate angular differential imaging (ADI), while each target was observed with an identical instrument, filter, and dither pattern, forming a self-consistent library of reference PSFs to to facilitate reference differential imaging (RDI). The narrow band of F656N was also helpful in reducing chromatic variations in the assembled PSF library.

For J1604, 12 Hα images were taken over 2 epochs (of 8 and 4 images, respectively) from the period of February 22nd to April 15th, 2022. The total exposure time for these data images was 5,328 seconds, with 444 seconds per exposure. A set of four dithered images are interlaced in Fourier space following procedures described in **?** and implemented in Y. Zhou et al. (2021) to form Nyquist sampled images (pixel scale = 20 mas). In these images, the host star has approximately 17,000 electron counts. The other observations obtained by the GO-16651 program were processed in the same way. For all RDI observations, the complete library of 80 reference PSFs was used.

3. KLIPTONITE IMAGE PROCESSING

Our methodology in evaluating the quality of PSF-subtracted images closely follows that which is described in J. I. Adams Redai et al. (2023), but with a few adjustments. The original method focuses on identifying the highest quality ground-based direct imaging results in the absence of foreknowledge of disk features, while our method is built for optimizing the probability of detecting suspected planets within disks of interest, especially given position and mass estimates. Therefore, we can generally operate within a smaller parameter space, and make use of tools like false-signal injection to produce a more robust signal-to-noise map of expected results without the need to probe for false positives. The process is discussed in more detail in Section 3.1.

In general, the KLIP algorithm takes a number of parameters that control the "aggressiveness"[2] of the subtraction. A more aggressive reduction will model and subtract the stellar PSF more easily, reducing noise, but risks self-subtraction of other astrophysical sources in the disk. Therefore, a more aggressive reduction may also lower the retrieved signal.

3.1. *Point-Source Reductions*

KLIPtonite uses different approaches to find the optimal KLIP parameters for detecting point sources versus evaluating disk morphology, but the relevant subtraction parameters are identically `movement`, `nAnnuli`, and `numbasis`. When the target astrophysical source in the image is a point-source (such as a protoplanet or brown dwarf), KLIPtonite takes these inputs:

[2] see the pyKLIP documentation for more explanation of this terminology.

Table 1. KLIP optimization parameters, their definitions, and their default values for KLIPtonite optimizations.

Parameter	Definition	KLIPtonite Default Array
`movement`	Number of pixels a potential astrophysical source moves due to motion of the observational instrument	`[1,2,3]`
`nAnnuli`	Number of different annuli that the image will be divided into during subtraction (annuli follow log spacing)	`[1,2,3,4,5,6,7,8,9,10,11,12,13,14,15]`
`numbasis`	Number of basis vectors for the model PSF that will be subtracted	`[1,2,3,4,5,10,15,20,25,30,35,40,50,75,100]`

1. Unsubtracted input images;
2. PSF subtraction mode ('ADI', 'RDI', or 'ADI + RDI');
3. A library of PSF images (if 'RDI' is selected)
4. Desired test location and contrast ratio for a point source;
5. Three lists of `pyKLIP` control parameters with specified values: `movement`, `nAnnuli`, `numbasis`

Given these, the program uses the `pyKLIP` fakes module in combination with Photutils (L. Bradley et al. 2024) to inject simulated planet signal at a particular contrast ratio. Once the dataset is injected, the program loops the data through all possible combinations of PSF subtraction parameters. Once a full dataset of subtracted images is assembled, it calculates the signal-to-noise of the injected signal in each image, then finally assembles a three-dimensional KLIPtonite quality matrix. Each of the three axes of the KLIPtonite quality matrix represents one of the `pyKLIP` control parameters, and each cell contains a value from 0 to 1, which is the quality metric for the image reduced with that combination of parameters.

Before assembling this quality matrix, both the signal and the noise within each image need to be calculated. For point-source reductions, the method of retrieving the noise in each image is similar to the method described by D. Mawet et al. (2014) — the program begins by packing as many circular sub-annuli as possible within the same separation as the injection location, then sums the total flux within each of these regions, and takes the mean and standard deviations of these values. The mean becomes the background within the image, and the standard deviation becomes the noise. KLIPtonite evaluates the retrieved signal in each image by integrating flux within a circular aperture and then subtracting the calculated background. The radius of the noise subannuli and the signal aperture are both equivalent to the filter full-width at half-maximum.

From here, evaluating the normalized noise quality metric is rather simple. The quality matrix is calculated from the matrix with entries composed of the quotients of the elements at the corresponding locations in the signal matrix and the noise matrix (S/N). For example, if $S_{i,j,k}$ is the entry in the signal matrix at $[i,j,k]$, and $N_{i,j,k}$ is the entry in the noise matrix at $[i,j,k]$, the corresponding matrix element $C_{i,j,k} = \frac{S_{i,j,k}}{N_{i,j,k}}$. Entries in the matrix C are then transformed into the quality matrix Q according to this formula (J. I. Adams Redai et al. 2023):

$$Q_{i,j,k} = \frac{\log_{10}(C_{i,j,k}) - \log_{10}(C_{\min})}{\log_{10}(C_{\max}) - \log_{10}(C_{\min})}$$

After this is done, the values in the quality matrices take values from 0.0 to 1.0, but some cells may contain not-a-number (NaN) values. These are excluded from minima calculations and correspond to a non-retrieval of the expected

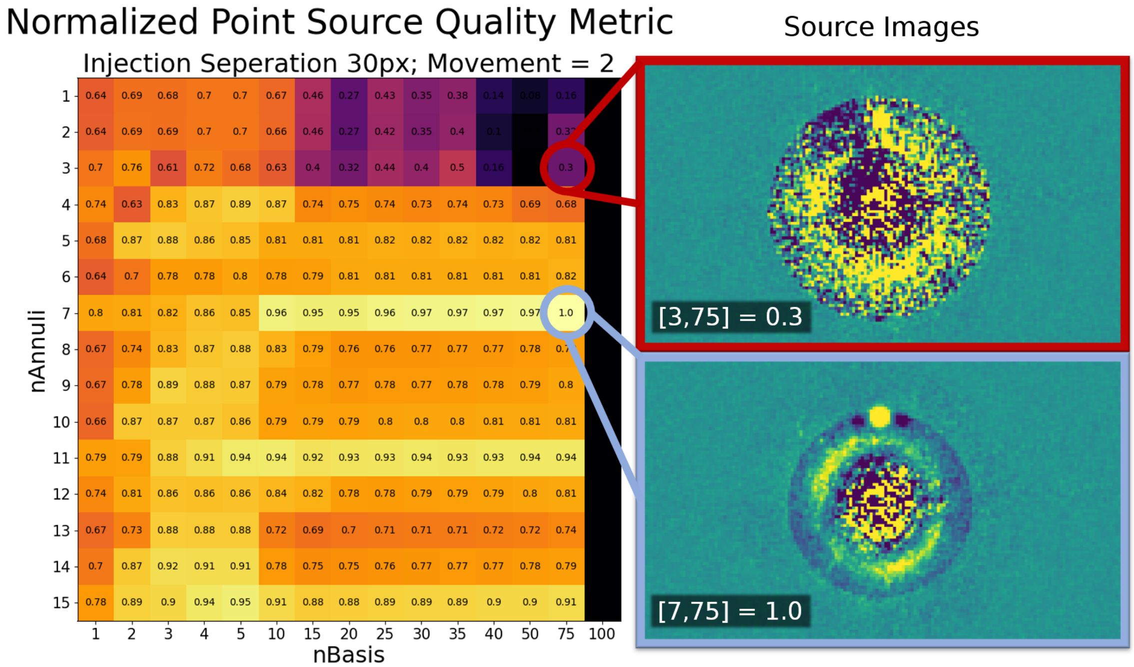

Figure 1. *Left*: Slice of KLIPtonite quality matrix for a point source in the J1604 disk at a contrast ratio of 10^{-3}, a separation of 30 pixels (0.60"), and a position angle of 0°. *Right*: The respective PSF-subtracted images for the indicated cells.

planetary signal in the image. More precisely, they indicate the position of a negative value for the retrieved signal, since when the logarithm of these values is taken, a NaN value is returned. (The right column of the example matrix is composed entirely of NaN values. This is because KLIPtonite defaults to setting 100 as the maximum number of basis vectors in its reductions, and if there are fewer than 100 RDI library files available for reduction, images reduced with basis vector counts higher than the number of available basis-vector images will be entirely composed of NaNs.)

3.2. *Disk-Source Reductions*

When the target astrophysical source in the image is the protoplanetary disk itself, KLIPtonite takes these inputs:

1. Unsubtracted input images;
2. PSF subtraction mode ('ADI', 'RDI', or 'ADI + RDI');
3. A library of PSF images (if 'RDI' is selected)
4. The location of disk signal [inner radius, bounding radius) and disk noise bounds [bounding radius, outer radius];
5. pyKLIP control parameters: movement, nAnnuli, numbasis

Disk-source data processing with KLIPtonite is easier, but it can also be rather crude. For disks, the signal in each image is considered to be the mean value of single-pixel flux between two annuli, referred to as the inner radius and the bounding radius. The noise in each image is then considered to be the standard deviation of single-pixel flux between the bounding radius and another annulus, the outer radius. Together, these three annuli form two distinct regions, a signal region and a noise region, which touch but do not overlap. So, for disk processing with KLIPtonite, a solid understanding of the disk geometry (such as the location of regions of interest) is required before any data processing begins. Obtaining a lower-quality "quick" reduction via `kliptonite.red.quick()` or other methods may be a necessary precursor to actual data processing.

The disk quality metric is defined in the same way as the point-source quality metric; it is nothing but the normalized log-space signal-to-noise. However, for disk processing, special care needs to be taken when evaluating quality metric results, since the result is far more sensitive to the selected annulus geometry. For example, if a pyKLIP reduction

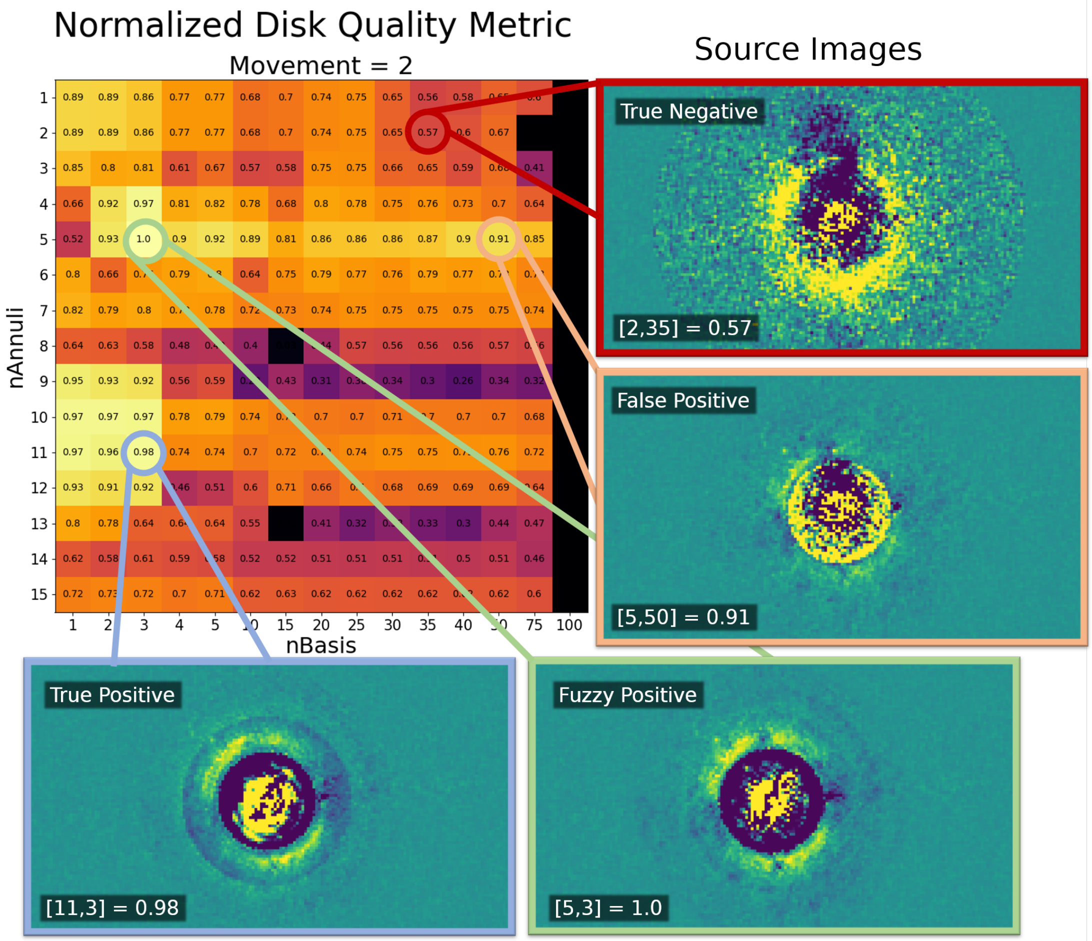

Figure 2. *Left*: Slice of KLIPtonite quality matrix for the J1604 disk itself, optimized for a disk at a separation of 19 pixels (0.38”) and with a bounding radius of 10 pixels (0.20”). *Right* and *Lower*: PSF subtraction results, some of which demonstrate false or fuzzy positives.

annulus overlaps with the bounding radius, noise may be much higher in the signal region than in the noise region, leading to a false positive where the noise in the target image is grossly undervalued. This will cause the whole row of images associated with that value of **`nAnnuli`** to have inflated quality metrics, as demonstrated in Figure 2. Careful attention ought to be paid to make sure disk processing results properly reflect image quality.

4. RESULTS

4.1. *Disk Morphology*

For the purpose of analysis, the chosen KLIPtonite-optimized disk reduction was an ADI + RDI reduction with a movement of 2 pixels, an annulus count of 11, and a basis vector count of 3, presented in Figure 3. This reduction was chosen for its high signal-to-noise ratio (image quality metric: 0.98), as well as the more appropriate separation between the KLIP annuli and the region of interest.[3] In this reduction, we find the peak total flux in Hα to be located at a separation of 23 pixels (0.46”), or 69 AU.

To better evaluate the dimensions of the shadows identified by P. Pinilla et al. (2018), the region of interest was transformed into a number of 1-dimensional binned slices in $(\theta, \Sigma_{\rm counts})$, where the latter is the total flux in each

[3] Recall that, for some reductions, the boundaries between KLIP annuli closely overlap with the location of the main disk, leading to an increased risk of non-physical subtraction close to the physical disk. See Section 3.2.

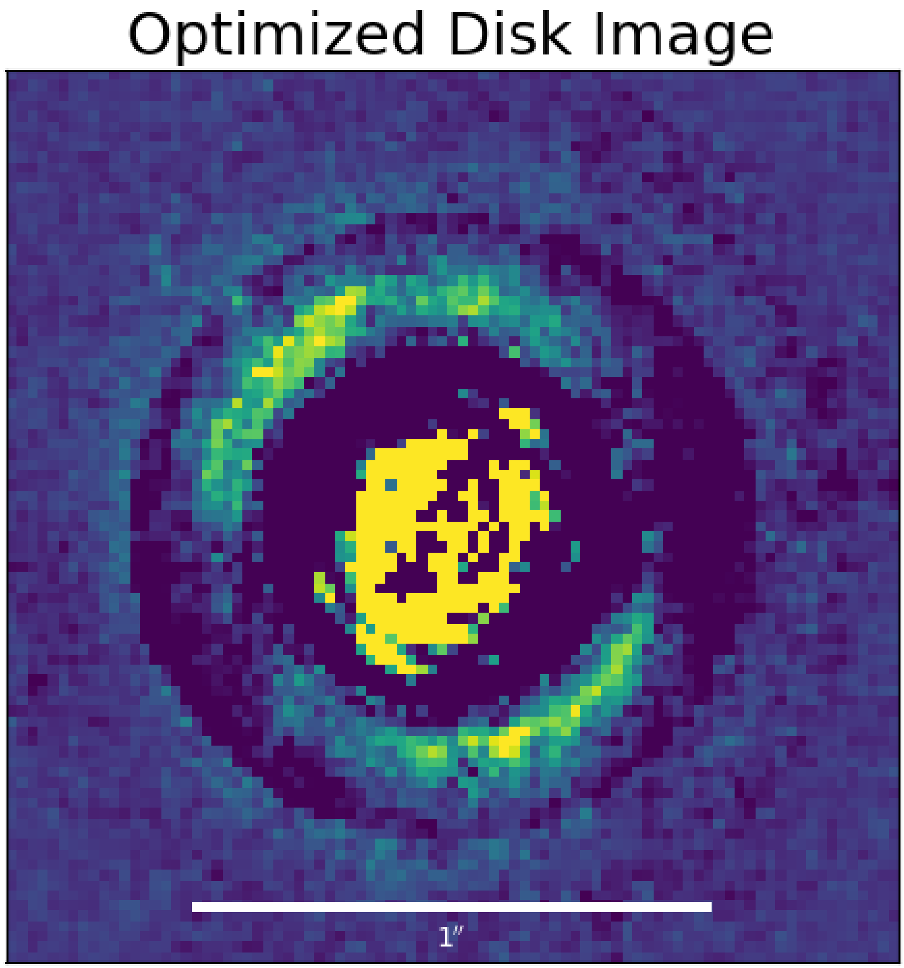

Figure 3. The KLIPtonite-optimized disk image of J1604 (2,11,3) chosen for morphological analysis.

slice, as visualized in Figure 5. In Figure 6, we can confirm that the deeper and thinner gap appears at a position angle close to 90°, while the wider, more shallow gap appears at a position angle close to 250°. However, we were unable to confirm the variability of the shadows. Regardless, the dimensionality of the 90°gap is intriguing, as the normalized total flux stays relatively low for longer than anticipated, and in a region of the image that is robust to non-physical influences like diffraction spikes.

We would also like to comment on the increase in local flux at the separation of roughly 30 pixels and a position angle of around 45°. This is likely nonphysical, as it appears in only the latter epoch of our reductions (though it does appear in every image).

4.2. *Planet Detection Sensitivity*

To evaluate detectability, we injected 25 different magnitudes of false signal into the data set and attempted to retrieve the injected signal through KLIPtonite-optimized PSF-subtractions. The injected magnitude in each reduction was

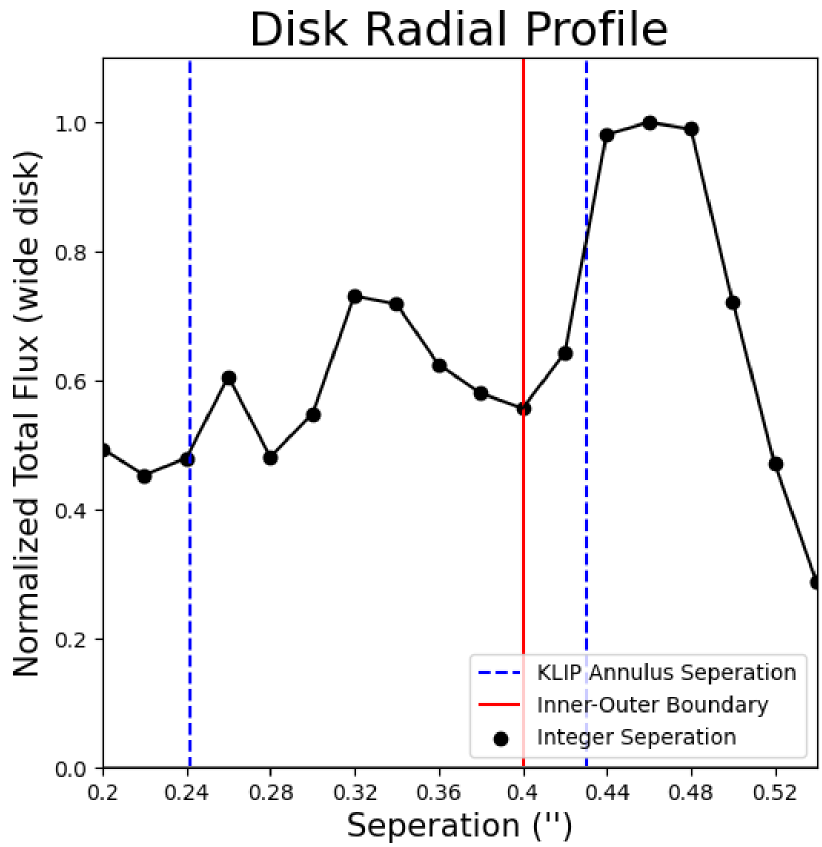

Figure 4. The total normalized flux at each integer pixel separation. The separation marked "inner-outer boundary" denotes the rough boundary of physicality in the disk morphology, as the location of the secondary peak (here at 0.32") is highly variable across reductions.

calculated following the relation for accretion luminosity:

$$L_{\rm acc} = \frac{GM\dot{M}}{R}$$

and under the assumption that the magnitude of Hα luminosity follows directly from the accretion luminosity after the relation outlined in Y. Aoyama et al. (2021), namely:

$$\log_{10}(L_{\rm acc}/L_{\odot}) = 0.95 \cdot \log_{10}(L_{\rm H\alpha}/L_{\odot}) + 1.61$$

In order to best evaluate the detectability of the injected planet, we applied KLIPtonite optimization to each instance of PSF-subtraction and retrieved only the reductions with the highest respective quality metrics. This resulted in considerable improvements in signal-to-noise from the initial test reduction, and the corresponding values are shown in Figure 8. In general, optimized results had more than $4\times$ higher values of signal-to-noise compared to our initial reductions.

We find that a 5σ detection is possible with an accretion rate as low as 10^{-8} $\rm M_{jup} \cdot yr^{-1}$, but only at a starting mass of at least 2 $\rm M_{jup}$. Any planet of at least two Jupiter-masses accreting at at least $10^{-8}\rm M_{jup} \cdot yr^{-1}$ is highly detectable with a significance of more than 5σ.

5. CONCLUSION

We have demonstrated the use of a powerful new method for optimizing the signal-to-noise ratio of PSF subtraction results for space-based direct imaging, and applied this method to calculate the boundaries of planet detection in

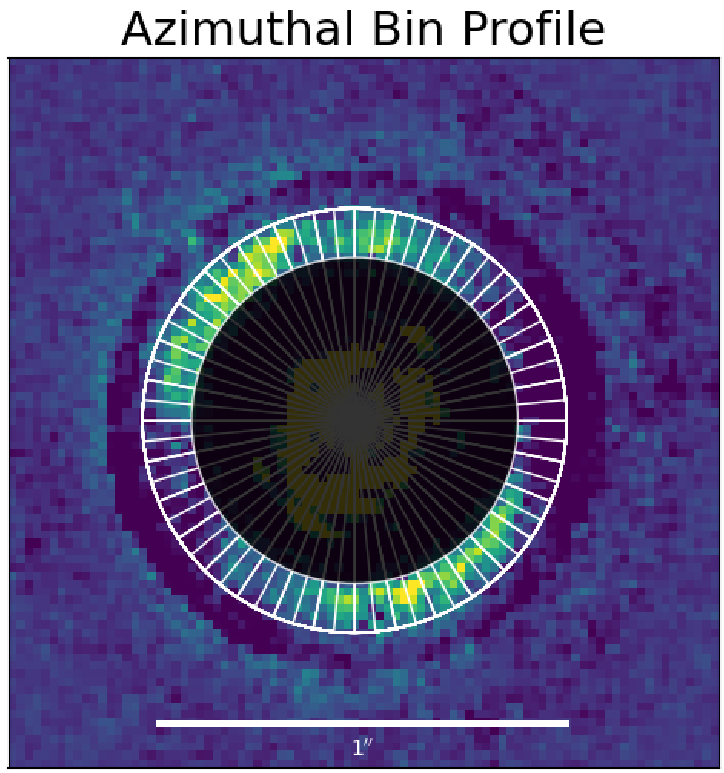

Figure 5. Visual representation of the 2-dimensional disk bins.

Hubble data from the J1604 disk. This calculation set a terminal observable accretion rate in the Hα wavelength at $10^{-8}\mathrm{M}_{\mathrm{jup}} \cdot \mathrm{yr}^{-1}$.

We have also used a modified version of this method to create deep-epoch images of the J1604 disk and confirm the features observed by previous studies in the Hα wavelength, namely, the separation of peak flux, the separation of the main outer disk, and the dimensionality of the disk's astrophysical shadows.

Facilities: HST(WFC3)

Software: NumPy (C. R. Harris et al. 2020), Matplotlib (J. D. Hunter 2007), Astropy (Astropy Collaboration et al. 2013, 2018, 2022), Photutils (L. Bradley et al. 2024), pyKLIP (J. J. Wang et al. 2015)

REFERENCES

Adams Redai, J. I., Follette, K. B., Wang, J., et al. 2023, AJ, 165, 57, doi: 10.3847/1538-3881/aca60d

Aoyama, Y., Marleau, G.-D., Ikoma, M., & Mordasini, C. 2021, ApJL, 917, L30, doi: 10.3847/2041-8213/ac19bd

Astropy Collaboration, Robitaille, T. P., Tollerud, E. J., et al. 2013, A&A, 558, A33, doi: 10.1051/0004-6361/201322068

Astropy Collaboration, Price-Whelan, A. M., Sipőcz, B. M., et al. 2018, AJ, 156, 123, doi: 10.3847/1538-3881/aabc4f

Astropy Collaboration, Price-Whelan, A. M., Lim, P. L., et al. 2022, ApJ, 935, 167, doi: 10.3847/1538-4357/ac7c74

Boccaletti, A., Di Folco, E., Pantin, E., et al. 2020, Astronomy amp; Astrophysics, 637, L5, doi: 10.1051/0004-6361/202038008

Bradley, L., Sipőcz, B., Robitaille, T., et al. 2024,, 2.0.2 Zenodo, doi: 10.5281/zenodo.13989456

Close, L. M. 2020, AJ, 160, 221, doi: 10.3847/1538-3881/abb375

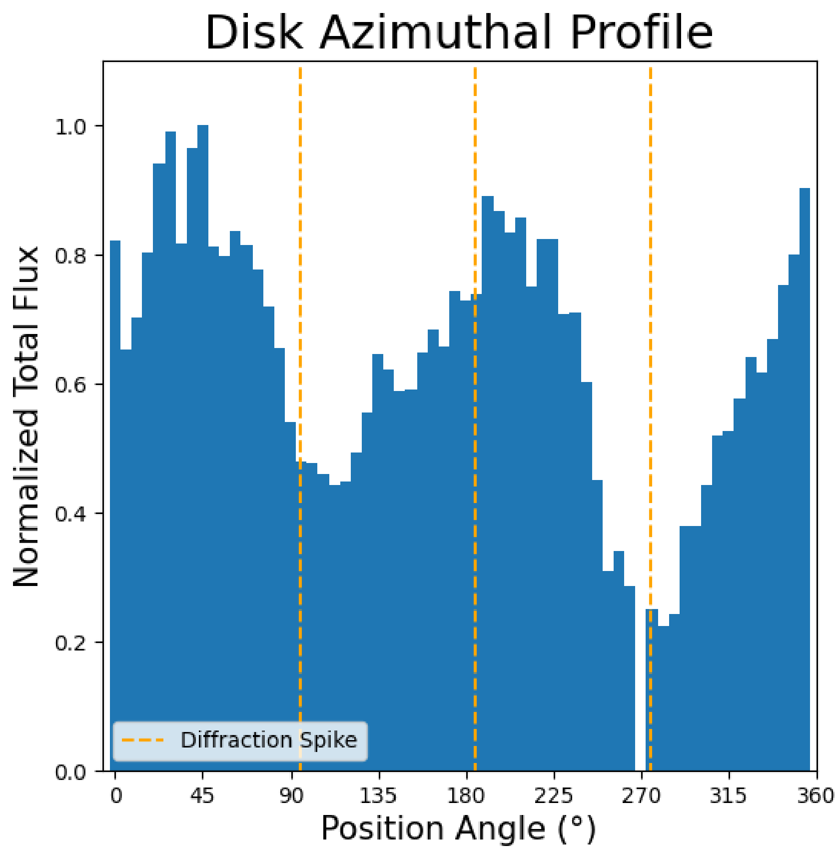

Figure 6. Binned azimuthal profile of the main J1604 disk.

de Juan Ovelar, M., Min, M., Dominik, C., et al. 2013, A&A, 560, A111, doi: 10.1051/0004-6361/201322218

Francis, L., & van der Marel, N. 2020, The Astrophysical Journal, 892, 111, doi: 10.3847/1538-4357/ab7b63

Haffert, S. Y., Bohn, A. J., de Boer, J., et al. 2019, Nature Astronomy, 3, 749, doi: 10.1038/s41550-019-0780-5

Harris, C. R., Millman, K. J., van der Walt, S. J., et al. 2020, Nature, 585, 357, doi: 10.1038/s41586-020-2649-2

Hunter, J. D. 2007, Computing in Science & Engineering, 9, 90, doi: 10.1109/MCSE.2007.55

Keppler, M., Benisty, M., Müller, A., et al. 2018, A&A, 617, A44, doi: 10.1051/0004-6361/201832957

Mawet, D., Milli, J., Wahhaj, Z., et al. 2014, ApJ, 792, 97, doi: 10.1088/0004-637X/792/2/97

Pinilla, P., Benisty, M., de Boer, J., et al. 2018, ApJ, 868, 85, doi: 10.3847/1538-4357/aae824

Stadler, J., Benisty, M., Izquierdo, A., et al. 2023, Astronomy amp; Astrophysics, 670, L1, doi: 10.1051/0004-6361/202245381

Stolker, T., Bonse, M. J., Quanz, S. P., et al. 2019, A&A, 621, A59, doi: 10.1051/0004-6361/201834136

Wang, J. J., Ruffio, J.-B., De Rosa, R. J., et al. 2015,, Astrophysics Source Code Library, record ascl:1506.001

Zhou, Y., Herczeg, G. J., Kraus, A. L., Metchev, S., & Cruz, K. L. 2014, ApJL, 783, L17, doi: 10.1088/2041-8205/783/1/L17

Zhou, Y., Bowler, B. P., Wagner, K. R., et al. 2021, AJ, 161, 244, doi: 10.3847/1538-3881/abeb7a

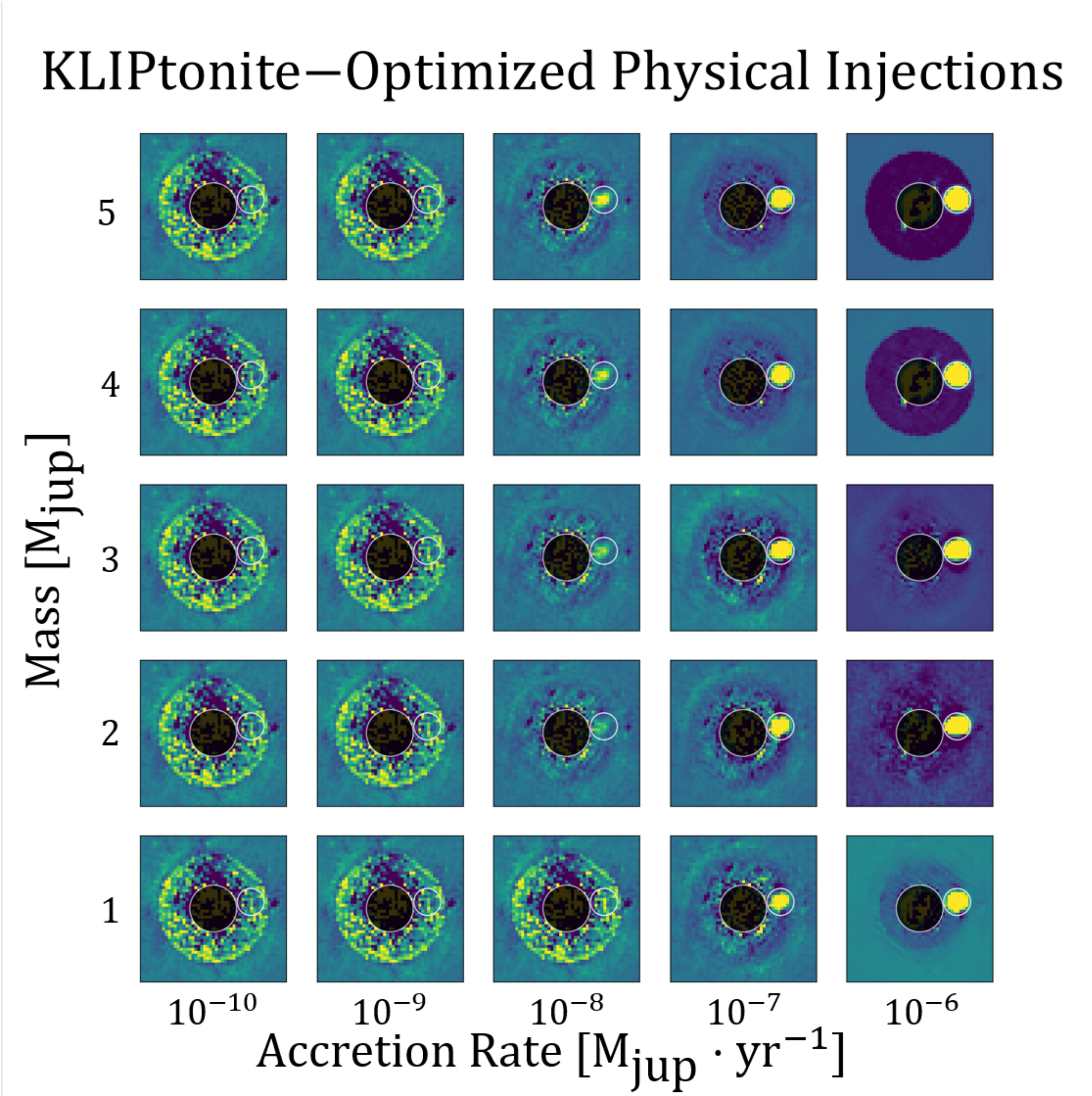

Figure 7. KLIPtonite-optimized PSF-subtractions with injections of physically motivated signals with different accretion parameters. Note the the 5σ boundary calculated for a 2 M_{jup} planet at an accretion rate of 10^{-8} $M_{jup} \cdot yr^{-1}$.

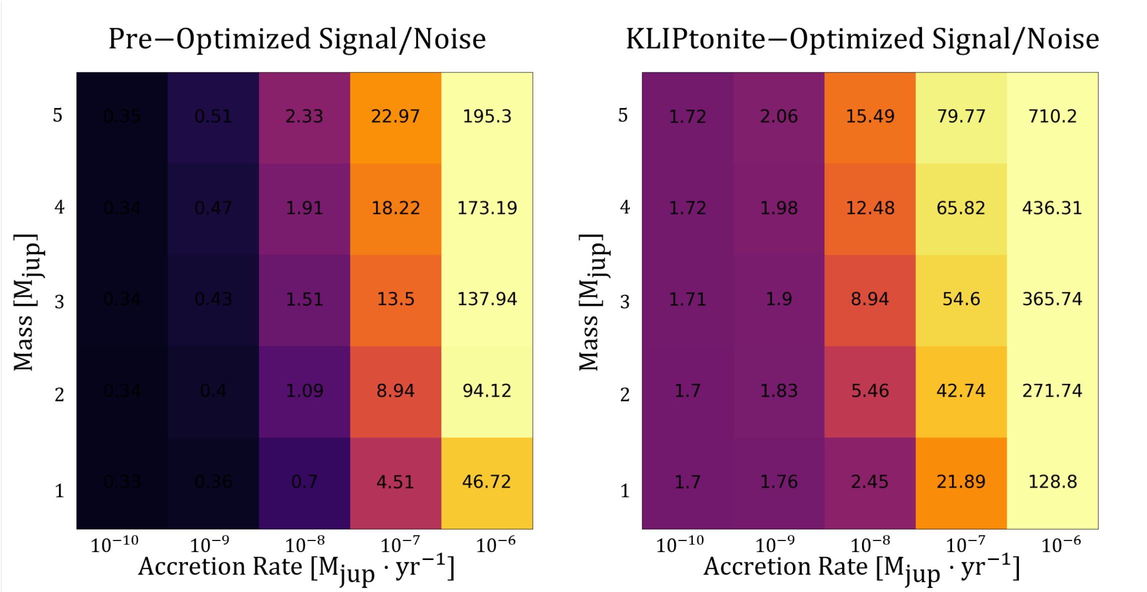

Figure 8. A comparison of the peak signal-to-noise values of our initial suite of test subtractions, all done at (1,3,50), against the same dataset subtracted using KLIPtonite-optimized parameters.